Genotypic variation in maize leaf senescence after ear removal is caused by excess accumulation of photosynthates

Jie Yuan[1,2#], Fengying Duan[1#], Kaijian Fan[1], Yanfang Heng[1], Xuxiang Wang[1], Yupeng Zhou[1], Qiang He[1], Shaobo Wei[1], Xuefang Sun[2], Liang Li[1], Xia Li[1*], Wenbin Zhou[1*]

[1]State Key Laboratory of Crop Gene Resources and Breeding, Institute of Crop Sciences, Chinese Academy of Agricultural Sciences, Beijing 100081, China

[2]College of Agronomy, Qingdao Agricultural University, Qingdao, 266109, China

[#] These authors contributed equally to this work.

* To whom correspondence should be addressed:

Tel: +86 10 82107841; Email: zhouwenbin@caas.cn; lixia06@caas.cn

Short title: Genotypic variation in maize leaf senescence

The author responsible for distribution of materials integral to the findings presented in this article in accordance with the policy described in the Instructions for Authors (https://academic.oup.com/plphys/pages/General-Instructions) is Wenbin Zhou.

Abstract

Leaf senescence is a key developmental process influencing photosynthesis, carbon allocation, and crop productivity, all tightly regulated by source–sink balance. In maize (*Zea mays*), abscisic acid (ABA) signaling and non-structural carbohydrate (NSC) partitioning have been proposed as major determinants of senescence timing under sink limitation. Through multi-year, multi-genotype analyses, we refine the current understanding by identifying starch-induced chloroplast disruption as the primary trigger of sink-removal-induced senescence, whereas ABA acts mainly as a secondary, modulatory signal. We also reveal a respiration-linked metabolic compensation mechanism that stabilizes leaf function in genotypes with delayed senescence. In early-senescing genotypes, ear removal induced significant chlorophyll loss, anthocyanin accumulation, and severe sugar/starch overaccumulation that disrupted chloroplast ultrastructure, coinciding with reduced leaf protein contents and impaired photosynthesis. By contrast, genotypes with delayed senescence maintained pigment stability, displaying enhanced dark respiration, balanced carbohydrate metabolism, and chloroplast integrity. Shading experiments further confirmed that starch overaccumulation, rather than ABA elevation, is the dominant driver of sink-removal-induced senescence. Metabolomic analyses showed that early-senescing genotypes accumulate soluble sugars and phosphoenolpyruvate (PEP)-pathway intermediates, whereas genotypes with delayed senescence exhibited reduced tricarboxylic acid (TCA) cycle activity and elevated aspartate-family amino acids. Transcriptomics revealed downregulation of sucrose transporters (e.g., *ZmSUT7*) and starch degradation genes (e.g., *ZmBmy3*) alongside upregulation of anthocyanin and carbohydrate metabolism genes in early-senescing genotypes. Co-expression network analysis further identified hub genes associated with carbohydrate and amino acid metabolism, linking transcriptional regulation to genotype-specific metabolic adjustments. Together, these findings refine current source–sink regulatory models and offer potential physiological and metabolic targets for improving source–sink coordination and enhancing yield resilience in maize.

Keywords: Sink removal; source-sink imbalance; leaf senescence; maize

Introduction

Leaf senescence is a finely regulated degenerative process that plays a critical role in nutrient recycling and remobilization to developing organs, thereby significantly influencing crop growth and yield formation (Guo *et al.*, 2021). Senescence is orchestrated by an intricate network of internal signals, including hormones such as cytokinin, abscisic acid (ABA), ethylene, salicylic acid (SA), gibberellic acid (GA), and auxins, as well as carbohydrate signaling, which can act in a context-dependent manner to either promote or delay senescence (Ahmad and Guo, 2019; Woo *et al.*, 2019; Kim, 2019; Asad *et al.*, 2024).

A central determinant of senescence onset is the source–sink relationship, which governs the allocation of photoassimilates from photosynthetic tissues (sources) to developing or storage organs (sinks) (Mason and Maskell, 1928 ; Rosado-Souza *et al.*, 2023; Smith *et al.*, 2018). The efficiency of this process depends on phloem transport (flow) and is influenced by the strength of the source (*e.g.*, photosynthetic capacity, nutrient uptake) and sink demand (*e.g.*, metabolic capacity, storage activities) (Arp, 1991; De Schepper *et al.*, 2013). Enhancing both aspects synergistically boosts yield, as demonstrated by coordinated "push-pull" strategies that doubled tuber yield and starch accumulation in potato (Jonik *et al.*, 2012).

When source-sink balance is perturbed, senescence can be triggered prematurely. A weakened source may cause carbohydrate depletion, whereas reduced sink demand may lead to carbohydrate overaccumulation; in either case, homeostasis is disrupted and leaf senescence is accelerated (Muller *et al.*, 2011; Abeledo *et al.*, 2020). To probe these mechanisms, experimental manipulations such as ear or floral removal, fruit thinning, or altered temperature treatments have been widely applied. These studies revealed species-specific and genotype-dependent senescence responses (Lv *et al.*, 2020). For instance, pod removal in soybean delayed leaf senescence by maintaining chlorophyll and sugar levels (Zhang *et al.*, 2016; Yun *et al.*, 2020), with similar effects in sunflower, cowpeas, and wheat (Biswas and Mandal, 1986; Ho *et al.*, 1987; Khanna-Chopra and Reddy, 1988). In contrast,

sink removal in maize and barley often accelerates leaf senescence (Mandahar and Garg, 1975; Christensen *et al.*, 1981; Crafts-Brandner *et al.*, 1984).

Notably, senescence responses in maize are strongly genotype-dependent. For example, the inbred line B73 displays early senescence after ear removal, whereas Mo17 retains greenness (Ceppi *et al.*, 1987; Sekhon *et al.*, 2012). A broader screen identified only three stay-green inbred lines among 31 tested under non-pollinated conditions (Kumar *et al.*, 2019), highlighting substantial natural variation in this trait. Recent multi-omics studies in maize have advanced our understanding of source-sink regulated senescence, linking carbohydrate accumulation, trehalose-6-phosphate (T6P) signaling, and extensive transcriptomic reprogramming to senescence progression (Sekhon *et al.*, 2012; Wu *et al.*, 2018). These changes are accompanied by transcriptomic and metabolomic reprogramming in pathways related to proteolysis, oxidative stress, ABA signaling, and protein homeostasis (Kumar *et al.*, 2023). Nevertheless, the genetic and mechanistic basis underlying genotype-specific senescence responses to sink manipulation in maize remains poorly understood.

In this study, we investigated six maize genotypes with contrasting senescence behaviors under ear-removal conditions, exhibiting early- or delay-senescing phenotypes. By integrating physiological, anatomical, metabolomic and transcriptomic analyses, we dissected the mechanistic basis of these divergent responses and identified key regulatory pathways and candidate genes. Our findings offer insights into the genetic and metabolic regulation of source-sink regulated senescence and provide a foundation for improving source-sink coordination in maize breeding.

Results

Genotypic variation in maize leaf senescence following ear removal

To investigate genotypic variation in leaf senescence triggered by ear removal, six genetically distinct maize genotypes were selected for phenotypic and physiological characterization. Notably, the hybrid Xianyu 335 (XY335) and its parental lines, PH6WC

and PH4CV, exhibited clear signs of premature senescence following ear removal. By 19 days after treatment (DAT), their ear leaves had developed visible red pigmentation along the main veins, which intensified with time. By 25 DAT, most leaves had turned red and displayed extensive senescence. In contrast, the hybrid Zhengdan 958 (ZD958) and its parental lines, Zheng58 (Z58) and Chang7-2 (C7-2), showed no apparent phenotypic alterations, maintaining green leaf coloration throughout the experimental period and exhibiting a pronounced delay-senescing phenotype (Fig. 1A).

To quantitatively assess these phenotypic changes, pigment contents in ear leaves were measured. In XY335, PH6WC, and PH4CV, significant reductions in chlorophyll *a* (Chl *a*), chlorophyll *b* (Chl *b*), and carotenoid contents were observed under the ear removal (Ear-) treatment compared to the normally pollinated control (Ear+) at 25 DAT. Concurrently, anthocyanin content was markedly elevated under Ear- treatment in these genotypes (Fig. 1B-E). By contrast, pigment levels remained unaffected in Z58, C7-2, and ZD958. Time-course analysis of pigment ratios (Ear-/Ear+) further highlighted the divergent responses among the genotypes. In early-senescing genotypes (PH6WC, PH4CV, and XY335), total chlorophyll and carotenoids ratios began to decline at 19 DAT and fell to approximately 50% of Ear+ levels by 25 DAT (Supplementary Fig. S1A-B). This reduction was accompanied by a significant increase in anthocyanin accumulation—reaching over fourfold higher than Ear+ at 25 DAT (Supplementary Fig. S1C). In contrast, pigment content ratios remained largely stable in delay-senescing genotypes (Z58, C7-2, and ZD958) over the entire time course (Supplementary Fig. S1). Collectively, these results demonstrate that maize genotypes exhibit contrasting response to ear removal, separating early-senescing and delay-senescing groups, and suggesting differential regulation of source-sink balance and senescence pathways among maize genotypes.

Ear removal induced senescence is accompanied by a decline in photosynthetic capacity

To access the physiological consequences of pigment alterations on photosynthetic efficiency, gas exchange parameters were measured in ear leaves at 25 DAT. In the early-senescing genotypes (XY335, PH6WC, and PH4CV), ear removal significantly reduced net photosynthetic rate (P_n) by 40.82%, 64.01%, and 60.26%, respectively, relative to the Ear+ (Fig. 2A). These reductions were accompanied by significant declines in stomatal conductance (G_s) and transpiration rate (T_r), indicating impaired photosynthetic capacity.

In contrast, delay-senescing genotypes (Z58, C7-2, and ZD958) displayed no significant differences in P_n, G_s, intercellular CO_2 concentration (C_i), or T_r between the Ear- and Ear+ treatments at 25 DAT (Fig. 2A-D), highlighting their resilience to sink removal. Interestingly, these genotypes exhibited elevated nighttime dark respiration rates under Ear- treatment relative to Ear+, while no such respiratory increase was detected in the early-senescing genotypes, implying a compensatory mechanism to maintain carbon balance when sink demand is reduced (Fig. 2E).

Chloroplast ultrastructure is compromised during ear removal induced senescence

Given the central role of chloroplasts in photosynthesis and carbohydrate metabolism, transmission electron microscopy was employed to assess chloroplast ultrastructure in both bundle sheath cells (BSCs) and mesophyll cells (MCs) at 25 DAT. In the early-senescing genotypes (PH6WC, PH4CV, and XY335), Ear- treated leaves exhibited pronounced ultrastructural damage in BSC chloroplasts, including significant chloroplast enlargement, distorted shape, dislocation toward the cell center, and excessive accumulation of starch granule. Severe structural degradation was evident, with disrupted chloroplast bilayer membrane, degraded stroma lamellae, and leakage of chloroplast inclusions into the cytoplasm (Fig. 3A). By contrast, BSC chloroplasts in the delay-senescing genotypes

(Z58, C7-2, and ZD958) maintained typical ellipsoidal morphology with intact membrane and organized stroma lamellae structures under both Ear- and Ear+ conditions (Fig. 3B). Quantitative analyses further confirmed a reduction in the number of chloroplasts per BSC, along with increased starch granule and osmiophilic globule accumulation, specifically in the early-senescing genotypes (Fig. 3C-E).

Similar structural disruptions were also observed in MC chloroplasts of the early-senescing genotypes following ear removal. These chloroplasts became more spherical and showed thylakoid disorganization with reduced grana stacking, accompanied by marked increases in both starch grain size and osmiophilic globule abundance (Supplementary Fig. S2A). In contrast, MC chloroplasts in delay-senescing genotypes and in all Ear+ controls maintained spindle-shaped morphology with well-organized thylakoid membranes, fewer and smaller starch granules, and lower osmiophilic globule abundance (Supplementary Fig. S2A-E).

These results suggest that the sink removal triggers carbohydrate accumulation which disrupts chloroplast structure and integrity, accelerating senescence process in early-senescing genotypes. Importantly, despite these internal ultrastructural changes, no significant differences in overall leaf thickness or vascular bundle area were observed between Ear- and Ear+ treatments across six genotypes (Supplementary Fig. S3), indicating that the observed senescence is primarily driven by cellular and organelle-level disruptions rather than changes in gross leaf anatomy.

Excessive accumulation of photoassimilates acts as a trigger for ear removal induced leaf senescence

To elucidate the role of carbohydrate accumulation in Ear- induced senescence, we monitored sugar dynamics in ear leaves following ear removal across contrasting maize genotypes (Fig. 4). In early-senescing lines (XY335, PH6WC, and PH4CV), Ear- treatment led to significant and progressive accumulation of sucrose and starch starting from 9 DAT, followed by increases in glucose and fructose levels at 25 DAT (Supplementary Fig. S4).

In contrast, delay-senescing genotypes (Z58, C7-2, and ZD958) showed minimal changes in sugar contents throughout the treatment period (Fig. 4G-L; Supplementary Fig. S4).

Notably, the rise in sucrose content at 9 DAT preceded the sharp increase in anthocyanin levels at 25 DAT, suggesting that carbohydrate accumulation may act as a key upstream signal to activate anthocyanin biosynthesis and, ultimately, leaf senescence in susceptible genotypes (Supplementary Fig. S1C). To further test this hypothesis, a shading experiment was conducted on the early-senescing genotype XY335 immediately after Ear- treatment. By 30 DAT, phenotypic differences were evident: shaded regions of the leaf retained green coloration and high chlorophyll contents, while unshaded regions exhibited pronounced reddening, anthocyanin accumulation, and senescence symptoms (Fig. 5A-B).

Physiological and ultrastructural analyses demonstrated that unshaded regions exhibited elevated levels of sugar and starch, accompanied by enlarged and structurally compromised chloroplasts. These chloroplasts displayed disrupted thylakoid membranes, incomplete stroma lamellae, and an accumulation of excessive starch granules in both BSCs and MCs. In contrast, shaded regions maintained lower sugar contents and intact chloroplast ultrastructure (Fig. 5C-I), which was associated with delayed leaf senescence. These findings further highlight carbohydrate overaccumulation as a central regulator of sink-removal-induced senescence.

Ear removal modifies biomass allocation differently in early- and delay-senescing maize genotypes

To further explore the physiological consequences of Ear- induced senescence, we evaluated the biomass accumulation and partitioning among leaves, stems, and roots during the progression of leaf senescence following Ear- treatment. Leaf dry weight showed a significant increase only in PH6WC, whereas the other five genotypes displayed no significant differences compared to the Ear+ controls (Fig. 6A). Stem dry weights were increased significantly in PH6WC, PH4CV and XY335; while among the delay-

senescing genotypes, only C7-2 exhibited a significantly higher stem biomass relative to Ear+ group (Fig. 6B). Root dry weights were consistently elevated across all genotypes under Ear- treatment compared to their respective Ear+ groups (Fig. 6C).

Overall, total biomass (sum of leaves, stems, and roots) was enhanced across all genotypes in response to Ear- treatment. However, the magnitude of increase was greater in early-senescing genotypes (16.74%–32.73%) than in delay-senescing genotypes (6.64%–16.03%) (Fig. 6D). These results suggest that Ear- promotes biomass redistribution, particularly to roots and stems, with early-senescing genotypes showing more pronounced shifts in source-sink dynamics.

Abscisic acid accumulation does not drive ear removal induced leaf senescence

Abscisic acid (ABA) is widely recognized as a senescence-promoting hormone, particularly under stress conditions. To evaluate its role in Ear- induced senescence, we monitored dynamic changes in ABA content in maize leaves following Ear- treatment. At 1 DAT, ABA levels were significantly elevated in four genotypes (PH4CV, Z58, C7-2, and ZD958) compared with Ear+ controls, with this difference persisting until 9 DAT in PH4CV, C7-2, and ZD958 (Supplementary Fig. S5B, D, E, F). Furthermore, PH6WC also exhibited increased ABA levels by 9 DAT (Supplementary Fig. S5A). By 25 DAT, all six genotypes accumulated significantly higher ABA levels in response to the Ear- treatment (Supplementary Fig. S5).

However, the delay-senescing genotypes consistently showed higher ABA accumulation, despite displaying delayed or reduced senescence phenotypes. This discrepancy suggests that although ABA level is elevated during Ear- induced senescence, its accumulation may be a downstream consequence rather than a cause of the process. Therefore, ABA is likely not the primary regulator driving Ear- induced leaf senescence in maize.

Integrated metabolomic and transcriptomic analyses reveal candidate genes regulating source-sink dynamics in maize

To elucidate the molecular mechanisms underlying source-sink imbalance caused by ear removal, we performed time-course metabolomic and transcriptomic analyses on parental inbred lines representing early-senescing (PH6WC, PH4CV) and delay-senescing (Z58, C7-2) genotypes. Leaf samples were collected at 9, 19, and 25 DAT under Ear+ and Ear- conditions, based on physiological observations and previous studies to capture early molecular divergence prior to visible senescence (except 9 DAT for metabolomics).

Through untargeted metabolomic profiling, we detected 775 differential metabolites, including primary and secondary metabolites, across 19 and 25 DAT (Supplementary Table S1-S3). Principal component analysis (PCA) of metabolite profiles indicated that genotypes were the primary determinant of metabolic variation, with species-specific signatures prevailing over treatment or time-point effects (Supplementary Fig. S6A). This trend was further reflected in genotype-specific differences in metabolite abundance (Supplementary Fig. S6B). Metabolite profiling revealed an overall increase in sugar metabolism following Ear- treatment, particularly in early-senescing genotypes. Additionally, phosphoenolpyruvate (PEP) metabolism pathways were notably upregulated in these lines. In contrast, Ear- treatment in delay-senescing genotypes led to a reduction in tricarboxylic acid (TCA) cycle activity, accompanied by accumulation of aspartate family amino acids, suggesting a compensatory shift in energy metabolism (Supplementary Fig. S6C). These results highlight distinct metabolic reprogramming between early-senescing and delay-senescing genotypes in response to Ear- induced source-sink imbalance.

Transcriptomic profiling revealed a progressive increase in the number of differentially expressed genes (DEGs) over time, with 1,317 DEGs identified at 9 DAT, 5,934 at 19 DAT, and 17,325 at 25 DAT (Supplementary Fig. S7A; Supplementary Table S4-S7). Considering that senescence-related phenotypes became evident at 19 DAT, subsequent analyses focused on this time point. A set of 1,673 DEGs specifically associated with senescence responses in the early- senescence genotypes (PH6WC and PH4CV) (Supplementary Fig. S7B;

Supplementary Table S8) was enriched in pathway related to carbon metabolism, sugar and starch metabolism, membrane transport, and photosynthesis by Gene Ontology (GO) enrichment analysis (Fig. 7A-B).

K-means clustering analysis grouped the 1,673 DEGs into five distinct expression patterns (Fig. 7C). Among these, we focused on the consistently up-regulated and down-regulated clusters, as they likely represent core transcriptional responses to Ear-induced senescence (Supplementary Fig. S8-S13). Kyoto Encyclopedia of Genes and Genomes (KEGG) enrichment analysis revealed that up-regulated genes (Cluster 2) in early-senescing genotypes were strongly associated with anthocyanin biosynthesis, flavonoid metabolism, starch and sucrose metabolism, amino acid biosynthesis, and fatty acid degradation pathways (Supplementary Fig. S9). In contrast, down-regulated genes (Cluster 5) were predominantly enriched in photosynthesis-related pathways, including antenna protein biosynthesis (Supplementary Fig. S12). These contrasting expression patterns were consistent with the physiological observations: activation of secondary metabolism and carbon reallocation, together with suppression of photosynthetic processes, underpin the anthocyanin accumulation, chlorophyll decline, and reduced photosynthetic capacity observed in senescing leaves.

Further analysis identified several candidate regulatory genes with distinct expression patterns between early- and delay-senescing genotypes across time points (Supplementary Fig. S14). Among these, three key DEGs were identified: *ZmSUT7* (Zm00001eb402200), involved in sucrose transport; *ZmBmy3* (Zm00001eb016870), involved in starch degradation; and *ZmSGRL* (Zm00001eb076680), involved in chlorophyll breakdown. These genes were progressively down-regulated in early-senescing leaves, but remained relatively stable in delay-senescing genotypes (Fig. 7D-G). Similarly, SWEET family members (*ZmSWEET13a/b/c, ZmSWEET14a*) showed marked down-regulation in early-senescing genotypes, but only moderate decreases in delay-senescing lines (Fig. 7H-K). These transcriptional changes indicated that impaired sugar export and disrupted starch turnover play central roles in mediating Ear- induced leaf senescence.

To further explore regulatory networks associated with senescence following ear removal, weighted gene co-expression network analysis (WGCNA) was performed on 18,442 DEGs. A soft threshold power of 16 was selected for scale-free network construction, yielding 33 co-expression modules (Supplementary Fig. S15A). Module–trait association analysis revealed that the MEpink and MEturquoise modules were significantly positively correlated with delayed senescence and negatively correlated with early-senescing after Ear- treatment (Supplementary Fig. S15B-C). KEGG and GO enrichment analyses of hub genes (|MM| > 0.8, |GS| > 0.2) revealed that the MEturquoise module was strongly enriched in photosynthesis-related pathways (Supplementary Fig. S16), while the MEpink module was enriched in pathways associated with cell wall biosynthesis, cellulose degradation, and cellulose synthesis (Supplementary Fig. S17). Hub genes related to the senescence degree were identified based on weight values and intramodular connectivity (weight > 0.2 in MEturquoise; weight > 0.15 in MEpink). Among these, *Zm00001eb325370*, *Zm00001eb016250*, *Zm00001eb353810*, *Zm00001eb146750* and *Zm00001eb208970* showed high connectivity and were implicated in carbohydrate metabolism and amino acid metabolic processes (Supplementary Fig. S16, S17).

Discussion

Previous studies have shown that sink limitation in maize—whether induced by pollination prevention or ear removal—drives systemic physiological changes, including sugar overaccumulation, stress signaling activation, and premature leaf senescence, with substantial genotype-dependent variation (Ceppi et al., 1987; Kumar et al., 2019, 2023). These contrasting senescence responses reflect the intrinsically complex regulation of leaf aging, which integrates sugar metabolism, ABA and ROS signaling, and secondary metabolism. ABA and ROS have been proposed as early mediators of weakened sink demand, converging to trigger endoplasmic reticulum (ER) stress and lead to programmed cell death, further initiate senescence (Kumar et al., 2023). Meanwhile, the capacity to redirect accumulated non-structural carbohydrates (NSC) into secondary sinks is considered a major determinant of whether leaves senesce rapidly or maintain a stay-green

phenotype (Kumar et al., 2019). Central to this process is trehalose-6-phosphate (T6P), a sugar-signaling metabolite that modulates senescence via SnRK1 inhibition, thereby coupling carbohydrate status to developmental aging (Kumar et al., 2019; Zhang et al., 2009).

Building on these established foundations, our multi-year, multi-genotype analyses refine and extend current models of sink-removal-induced senescence by identifying additional regulatory layers. We show that starch overaccumulation and associated chloroplast disruption represent a decisive trigger of senescence; that ABA functions primarily as a secondary stress responder rather than a primary signal; and the enhanced dark respiration in delay-senescing genotypes provides a previously unrecognized metabolic strategy to mitigate carbon overload.

Although ABA is widely regarded as a major regulator of stress-induced senescence (Quiles *et al.*, 1995; Zhao *et al.*, 2022), previous work has further linked ABA accumulation under sink limitation to ROS-mediated ER stress and premature senescence in maize (Kumar *et al.*, 2023). Consistent with these findings, we observed elevated ABA levels following sink removal, but ABA alone does not determine differential senescence timing. ABA increased in both early- and delay-senescing genotypes—and even earlier in some delay-senescing lines (Supplementary Fig. S5)—indicating that its accumulation is a general stress response rather than a senescence trigger. Differences from prior studies—such as divergent ABA dynamics in B73 and Mo17 (Kumar et al., 2023)—likely reflect genotypic variation and methodological differences, as ear removal introduces mechanical injury whereas nonpollination preserves the cob as a transient sink. Consistent with this, KEGG analysis showed no enrichment of ABA-related pathways among senescence-associated DEGs (Supplementary Fig. S13). These findings collectively redefine ABA as a secondary, modulatory regulator rather than a determinative driver of sink-removal-induced senescence.

In contrast, carbohydrate signaling emerged as a dominant driver of senescence under source-sink imbalance. Ear removal induced significant sucrose accumulation beginning at 9 DAT, especially in early-senescing genotypes (Fig. 4), accompanied by downregulation of key sucrose transporter genes (*ZmSWEET13a/b/c* and *ZmSWEET14a*)

required for apoplastic phloem loading (Chen *et al.*, 2012; Bezrutczyk *et al.*, 2018). Impaired sugar export likely intensified carbohydrate overload and activated hexokinase (HXK1)-mediated sugar-signaling pathways (Smeekens *et al.*, 2010). Elevated sugar also promoted antioxidant flavonoid and anthocyanin biosynthesis—a conserved sugar-response pathway (LaFountain and Yuan, 2021; Ma *et al.*, 2021; Sunil and Shetty, 2022)—supported by the induction of flavonoid biosynthesis genes (Fig. 1E; Supplementary Fig. S8) and further verified by shading experiments (Fig. 5A–F). These findings support the view that excessive carbohydrate retention in leaves is a central driver of sink-removal-induced senescence.

A key finding of this study is the identification of starch, rather than soluble sugars alone, as a decisive mediator of premature senescence. Early-senescing genotypes accumulated excessive starch within chloroplasts (Fig. 3; Supplementary Fig. S2), coincident with repression of the starch degradation gene *ZmBmy3* and feedback inhibition of photosynthesis (Goldschmidt and Huber, 1992). Critically, starch overaccumulation severely disrupted chloroplast ultrastructure, leading to chloroplast swelling, thylakoid disorganization, and reduced protein content (Supplementary Fig. S18). Although similar phenotypes have been reported in starch metabolism mutants (Zhu *et al.*, 2020; Qin *et al.*, 2022), our work provides evidence that starch-induced chloroplast damage acts as a proximate trigger of senescence following sink removal in maize, functioning alongside, but distinct from, sugar- and ROS-mediated pathways (Fig. 4-5).

In contrast, delay-senescing genotypes exhibited markedly greater capacity to buffer carbon overload. Although both early- and delay-senescing genotypes redirected sugars into secondary sinks such as roots and stems (Fig. 6), consistent with prior studies (Kumar *et al.*, 2019; Sekhon *et al.*, 2019), this process occurred in both groups and therefore does not fully explain differences in senescence timing. Instead, our comparative analyses indicate that delayed senescence is additionally supported by a respiration-based compensatory mechanism. Delay-senescing genotypes exhibited higher dark respiration while maintaining photosynthetic capacity (Fig. 2A, 2E), enabling more effective consumption of excess carbon and preventing starch overaccumulation. This respiratory compensation helped

preserve chloroplast structure (Ren et al., 2024) and sustained functional greenness (Fig. 4G–L). By prolonging photosynthetic duration, delayed senescence enables continues allocation of assimilates to secondary sinks (e.g., late-developing kernels) or storage tissues such as stems and roots, reflecting positive metabolic flexibility and adaptive value under both sink-limited and normal conditions. This mechanism contributes to enhanced biomass stability and may benefit silage-type maize production.

Integrated transcriptomic and metabolomic analyses further revealed distinct metabolic architectures underlying these divergent senescence strategies. Consistent with previous studies showing that early-senescing lines accumulate more primary metabolites—such as sugar alcohols (e.g., mannitol, erythritol) and amino acids including phenylalanine and arginine—while stay-green lines preferentially accumulate secondary metabolites, such as phenylpropanoids and flavonoids (e.g., naringenin chalcone, eriodictyol) (Brar et al., 2025), our results confirm and extend these patterns under sink limitation. Following ear removal, early-senescing genotypes exhibited carbon-metabolic rigidity, accumulating TCA-cycle and PEP-pathway intermediates together with elevated sucrose and starch (Figs. 4A–F, S6). In contrast, delay-senescing genotypes maintained carbon homeostasis and redirected carbon into the aspartate family amino acids (lysine, isoleucine, methionine), reflecting a shift that competes with pyruvate entry into the TCA cycle (Galili, 2011). This reallocation reinforces carbon–nitrogen coupling, prevents accumulation of central carbon intermediates, and contributes to metabolic stability after sink disruption (Wu et al., 2018). Together with elevated respiration, these adjustments define the metabolic flexibility of delay-senescing genotypes.

Co-expression network analysis connected these physiological and metabolic differences to distinct regulatory modules. Delay-senescing genotypes showed enrichment of cell wall biosynthesis pathways and hub genes involved in carbohydrate and amino acid metabolism (Supplementary Fig. S15, S16, S17), consistent with the proposed roles of carbon partitioning into structural sinks for promoting stay-green traits in maize (Sekhon *et al.*, 2019). Notably, key senescence-related genes—including *ZmSUT7*, *ZmBmy3*, *ZmSGRL*, and

ZmSWEETs—showed stable or increased expression in delay-senescing lines but were strongly repressed in early-senescing genotypes (Fig. 7D–K). These contrasting patterns align with observed differences in sucrose export, starch degradation (Fig. 4A–F), and chlorophyll retention (Fig. 1B–D; Kumar et al., 2023), identifying these genes as strong candidates for functional validation of stay-green mechanisms in maize.

In conclusion, while previous studies identified several responses to sink removal, our multi-year, multi-omics analyses reveal mechanistic distinctions between early- and delay-senescing maize genotypes under sink limitation. Early-senescing lines (XY335, PH6WC, and PH4CV) exhibited impaired sucrose export, starch overaccumulation, chloroplast damage, and accelerated senescence; whereas delay-senescing lines (ZD958, Z58, and C7-2) maintained metabolic homeostasis through enhanced respiration and stable regulation of key transport and metabolic genes (Fig. 8). Together, these findings (i) refine ABA's role to a secondary regulator, (ii) identify starch-induced chloroplast damage as a key initiator of premature senescence, (iii) establish respiration-based metabolic compensation as a determinant of delayed senescence, and (iv) highlight candidate regulatory genes involved in source-sink balance. Although focused on two widely cultivated hybrids ZD958 and XY335 and their parental lines, and thus may not fully capture the diversity of senescence response across all maize genotypes, our work broadens current source-sink regulatory models and provides promising targets for improving photosynthetic longevity and yield stability in maize.

Materials and methods

Plant materials and experimental design

Six maize (*Zea mays* L.) genotypes were used in this study, including Xianyu335 (XY335), PH6WC, PH4CV, Zhengdan958 (ZD958), Zheng58 (Z58), and Chang7-2(C7-2). Both XY335 and ZD958 are major maize hybrid varieties widely cultivated in China, with contrasting responses to ear removal. XY335 (including its parental inbred lines PH6WC and PH4CV) displays early leaf senescence following ear removal, while ZD958 (composed of parental lines Z58 and C7-2) exhibits a delay-senescing phenotype under the same condition.

Field trials were conducted during the summer of 2022–2024 in Beijing (N 40°10'47", E 116°14'49"), where the maize life cycle spans ~120 days. ZD958 reaches silking in ~55 days post-emergence, while XY335 silks 3–5 days later. Prior to silking, ears were bagged to prevent cross-pollination. Uniformly growing plants were tagged and pollinated on the same day after silking. Two treatments were applied: Ear+ (Control)–normal pollination without intervention, and Ear- (Ear Removal)–female ears were removed immediately after pollination. To investigate the impact of leaf shading after ear removal, approximately 1/4 of the ear leaf area was covered with tinfoil to impose shading.

The experiment followed a randomized block design with three biological replicates. Each plot measured 4.2 m ×2 m, with a planting density of 60 cm (row spacing) ×20 cm (plant spacing). Standard agronomic practices were used for irrigation, fertilization, and pest/disease/weed control.

In most experiments, each biological replicate was generated by pooling samples from three plants. For the shading experiment, protein content determination, gas exchange measurements, histological analysis, transmission electron microscopy and biomass accumulation and distribution assays, each biological replicate corresponded to an individual plant.

Pigment measurements

For both Ear+ and Ear- treatments, leaves at the ear position were collected at 1, 9, 19, and 25 days after treatment (DAT) and immediately frozen in liquid nitrogen. Chlorophyll and carotenoid were extracted with grounded leaf samples in 100% acetone under dim light. Absorbance value at 470, 644.8, and 661.6 nm were recorded using a spectrophotometer (Ultrospec 7000, Biochrom). Chlorophyll and carotenoid concentrations were determined as described by Lichtenthaler (1987).

Approximately 30 mg of fresh leaf tissue was ground and extracted in 450 µL acidified methanol (99:1 methanol:HCl). Anthocyanins were extracted by incubating the samples at 4°C in darkness for 10 h. After adding 300 µL deionized water and 750 µL chloroform, the mixture was centrifuged, and the absorbance of the supernatant was measured at 530 nm and 657 nm using a spectrophotometer (Ultrospec 7000, Biochrom, USA) as described previously (Nakata *et al.*, 2013).

Sugar and starch content measurements

Carbohydrate content was determined following Li *et al.* (2020). Leaves from normal pollination and ear removal treatments were sampled at 1, 9, 19 and 25 DAT, as well as from shaded and unshaded regions after 30 days of shading, then rapidly frozen in liquid nitrogen. ~ 50 mg of leaf tissue was extracted with 1 mL 80% (v/v) ethanol at 80°C for 30 min, centrifuged, and repeated twice. Supernatants were combined, vacuum-dried, dissolved in deionized water, and used to assay sucrose, fructose, and glucose using Sucrose, D-fructose and Glucose Assay Kits (Megazyme). Residual pellets were used for starch quantification with the Total Starch Assay Kit (Megazyme).

Protein content determination

Maize leaf samples were collected at 25 days after Ear- treatment. Samples from Ear+ group were collected at the same time. For protein extraction, 0.1 g of fresh leaf tissue was homogenized in 400 µL of protein extraction buffer. The homogenate was incubated with shaking at 40 rpm for 30 min at room temperature, followed by centrifugation at 12000 rpm for 20 min at 4°C. The supernatant was collected and protein concentration was determined using Quick Start Bradford Reagent (Bio-Rad, USA). All extraction procedures were performed on ice to maintain protein stability.

Gas exchange measurements

Gas exchange was measured with ear leaves on the 1st and 25th day after normal pollination and ear removal treatment, using the LI-6400XT system (LI−COR Inc., Lincoln, NE, USA), from 9:00–11:30 am under a photosynthetic photon flux density (PPFD) of 1500 µmol photons m^{-2} s^{-1}. Dark respiration (R_d) rates were assessed between 21:00–24:00 at 0 PPFD.

Histological analysis

Leaves collected at 25 DAT were cut into 15 ×5 mm sections and fixed in pre-cooled FAA (formaldehyde: acetic acid: ethanol = 5:5:90 (v/v)). Fixed tissues were paraffin-embedded, and sectioned (8 µm) using an ultrathin microtome (Ultra-cut R, Leica). Sections were then stained with Senna solid green and visualized under a light microscope (DM5500B, Leica). Leaf thickness and vascular bundle area were quantified using ImageJ software.

Transmission electron microscopy (TEM)

Leaf segments (1×1 mm) were collected at 25 DAT and 30 days after shading. Samples were immediately fixed in 2% glutaraldehyde (pH 7.2), then immersed in 1% osmium tetroxide at 4 ℃ for 20 h. Following dehydration in ethanol and acetone series, samples were then subjected to vacuum drying in propylene oxide for twice. After embedding and ultrathin sectioning, the samples were viewed with a transmission electron microscope (Hitachi H-7650). Quantitative analysis of chloroplasts, osmiophilic granules, and starch granules was conducted using ImageJ software.

Abscisic acid quantification

Abscisic acid content of ear leaves was measured at 1, 9 and 25 DAT according to the published protocol (Soualiou *et al.*, 2023).

Biomass accumulation and distribution

Six representative plants showing red leaf coloration after Ear- treatment were selected. Samples were initially dried at 110℃ for 15 min to deactivate enzymes, followed by oven-drying at 80℃ until achieving constant weight. Dry weight of root (RDW), stem (SDW), and leaf (LDW) were measured separately. Total biomass = RDW + SDW + LDW. Percentage of DW increase was calculated as: (total biomass in Ear- treatment – total biomass in Ear+ group) / total biomass in Ear+ group.

Metabolite profiling

Maize leaves sampled at 19 and 25 DAT were used for metabolite profiling. Leaf samples (20 mg) were lyophilized, extracted with a methanol/acetonitrile/water (2:2:1) solution containing deuterated internal standards, homogenized, sonicated, and centrifuged to obtain the supernatant for analysis, with QC samples prepared by pooling equal aliquots of

the extracts. Metabolites were identified by matching MS and MS/MS data (< 30 ppm) against databases including HMDB, MassBank, LipidMaps, mzCloud, and KEGG. Robust LOESS signal correction (QC-RLSC) was applied for data normalization to correct for systematic bias. The statistical significance of metabolites was assessed using a combination of criteria. *P* values were derived from appropriate hypothesis tests, while variable importance in projection (VIP) scores were obtained from orthogonal partial least squares-discriminant analysis (OPLS-DA). Additionally, fold change (FC) was calculated to quantify the magnitude of differences between groups. These metrics collectively evaluated the contribution and explanatory power of each metabolite in sample classification and discrimination, thereby facilitating the identification of potential biomarker metabolites. A metabolite was considered statistically significant when $P < 0.05$ and VIP > 1. Differential metabolites were further analyzed for pathway enrichment using MetaboAnalyst. The metabolites and their corresponding pathways were visualized using the KEGG Mapper tool.

Transcriptome analysis

Maize leaf samples were collected at 9, 19, and 25 DAT. Total RNA was extracted using TRIzol ® reagent (Invitrogen), and RNA-seq libraries were constructed by using the TruSeq Stranded mRNA LT Sample Prep Kit (Illumina, USA). Sequencing was performed on an Illumina HiSeq platform. Clean reads were aligned to the maize B73 reference genome (AGPv4) using HISAT2 (v2.1.0) (Kim *et al.*, 2015), and transcript abundance was quantified with StringTie (v1.3.3b) (Pertea *et al.*, 2015). Differential expression genes (DEGs) were identified with the DESeq2 R package (Love *et al.*, 2014), applying thresholds (*adj*. *P*-value < 0.05 and $|\log_2$ fold change$| \geq 1$) to identify statistically significantly different expression in Ear- treated maize versus normally pollinated (Ear+) plants. KEGG enrichment was conducted using clusterProfiler (Wu *et al.*, 2021). Weighted gene co-expression network analysis (WGCNA) was performed in R using the WGCNA package (Langfelder and Horvath, 2008), and the regulatory networks were visualized with Cytoscape. Raw sequence data

generated in this study have been deposited in the NCBI BioProject database under accession number PRJNA1340406.

Reverse transcription quantitative PCR (RT-qPCR)

Total RNA was extracted from leaves at 25 DAT using the TRIzol reagent (Invitrogen). For cDNA synthesis, 1 μg total RNA was used as template for reverse transcription following a two-step procedure using *Evo M-MLV* RT Mix Kit with gDNA Clean for RT-qPCR (Accurate Biology, China). RT-qPCR was performed with SYBR Green *Pro Taq* HS premix on an ABI QuantStudio 6 Flex system (Applied Biosystems, USA). Primer sequences are listed in Supplementary Table S9.

Accession Numbers

The sequence data for the major genes discussed in this paper are available in the GenBank/EMBL databases under the following accession numbers: _ *ZmSUT7* (NM_001308124.1), *ZmBmy3* (XM_020546376.1), *ZmSGRL* (NM_001137437.1), *ZmSWEET13a* (NM_001155615.2), *ZmSWEET13b* (NM_001148182.1), *ZmSWEET13c* (NM_001147634.1), *ZmSWEET14a* (NM_001139364.1)

Funding

This work was supported by the Science and Technology Innovation 2030 Major Project (2024ZD0408002), the Key Program of National Natural Science Foundation of China (32330079), the Innovation Program of Chinese Academy of Agricultural Sciences (CAAS-CSIAF-202303 and CAAS-CSNCB-202302).

Author contributions

W.Z., L.L. and J.Y. conceived and designed the experiments. J.Y. performed most of the experiments and data collection. F.D., K.F., and Y.H. assisted in conducting field trials. Q.H., X.L., Y.Z. and X.W. were responsible for omics data analysis. S.W. and X.S. jointly participated in data interpretation J.Y., F.D., X.L. and W.Z. contributed to manuscript drafting.

Conflict of interest

The authors declare no conflicts of interest.

References

Abeledo LG, Savin R, Slafer GA (2020) Maize senescence under contrasting source-sink ratios during the grain filling period. Environ Exp Bot **180:** 104263

Ahmad S, Guo Y (2019) Signal transduction in leaf senescence: Progress and perspective. Plants **8:** 405

Arp WJ (1991) Effects of source-sink relations on photosynthetic acclimation to elevated CO_2. Plant, Cell Environ **14:** 869-875

Asad MAU, Yan Z, Zhou L, Guan X, Cheng F (2024) How abiotic stresses trigger sugar signaling to modulate leaf senescence? Plant Physiol Bioch **210:** 108650

Bezrutczyk M, Hartwig T, Horschman M, Char SN, Yang J, Yang B, Frommer WB, Sosso D (2018) Impaired phloem loading in *zmsweet13a,b,c* sucrose transporter triple knock-out mutants in *Zea mays*. New Phytol 218: 594-603

Biswas AK, Mandal SK (1986) Monocarpic senescence in wheat: Influence of sterile glumes and ear. Physiol Plantarum **67:** 431-434

Brar MS, Kumar R, Kunduru B, Leonard E, McMahan CS, Tharayil N, Sekhon RS (2025) Temporal analysis of physiological phenotypes identifies metabolic and genetic underpinnings of senescence in maize. Plant Cell **37:** koaf176

Ceppi D, Sala M, Gentinetta E, Verderio A, Motto M (1987) Genotype-dependent leaf senescence in maize: Inheritance and effects of pollination-prevention. Plant Physiol **85:** 720-725

Chen L, Qu X, Hou B, Sosso D, Osorio S, Fernie AR, Frommer WB (2012) Sucrose efflux mediated by SWEET proteins as a key step for phloem transport. Science 335: 207-211

Christensen LE, Below FE, Hageman RH (1981) The effects of ear removal on senescence and metabolism of maize. Plant Physiol **68:** 1180-1185

Crafts-Brandner SJ, Below FE, Wittenbach VA, Harper JE, Hageman RH (1984) Differential senescence of maize hybrids following ear removal: II. Selected leaf. Plant Physiol 74: 368-373

De Schepper V, De Swaef T, Bauweraerts I, Steppe K (2013) Phloem transport: a review of mechanisms and controls. J Exp Bot **64:** 4839-4850

Galili G (2011) The aspartate-family pathway of plants: linking production of essential amino acids with energy and stress regulation. Plant Signal Behav **6:**192-195

Goldschmidt EE, Huber SC (1992) Regulation of photosynthesis by end-product accumulation in leaves of plants storing starch, sucrose, and hexose sugars. Plant Physiol **99:** 1443-1448

Guo Y, Ren G, Zhang K, Li Z, Miao Y, Guo H (2021) Leaf senescence: progression, regulation, and application. Mol Hortic **1:** 5

Ho I, Below FE, Hageman RH (1987) Effect of head removal on leaf senescence of sunflower. Plant Physiol **83:** 844-848

Jonik C, Sonnewald U, Hajirezaei M-R, Flügge U-I, Ludewig F (2012) Simultaneous boosting of source and sink capacities doubles tuber starch yield of potato plants. Plant Biotechnol J 10: 1088-1098

Khanna-Chopra R, Reddy PV (1988) Regulation of leaf senescence by reproductive sink intensity in cowpea (*Vigna Unguiculata* L. Walp). Ann Bot **61:** 655-658

Kim D, Langmead B, Salzberg SL (2015) HISAT: a fast spliced aligner with low memory requirements. Nat Methods **12:** 357-360

Kim J (2019) Sugar metabolism as input signals and fuel for leaf senescence. Genes Genom **41:** 737-746

Kumar R, Bishop E, Bridges WC, Tharayil N, Sekhon RS (2019) Sugar partitioning and source-sink interaction are key determinants of leaf senescence in maize. Plant, Cell Environ **42:** 2597-2611

Kumar R, Brar MS, Kunduru B, Ackerman AJ, Yang Y, Luo F, Saski CA, Bridges WC, de Leon N, McMahan C, Kaeppler SM, Sekhon RS (2023) Genetic architecture of source-sink-regulated senescence in maize. Plant Physiol 193: 2459-2479

LaFountain AM, Yuan YW (2021) Repressors of anthocyanin biosynthesis. New Phytol **231:** 933-949

Langfelder P, Horvath S (2008) WGCNA: an R package for weighted correlation network analysis. BMC Bioinformatics **9:** 559

Li X, Wang P, Li J, Wei S, Yan Y, Yang J, Zhao M, Langdale JA, Zhou W (2020) Maize *GOLDEN2-LIKE* genes enhance biomass and grain yields in rice by improving photosynthesis and reducing photoinhibition. Commun Biol 3: 151

Lichtenthaler HK (1987) Chlorophylls and carotenoids: Pigments of photosynthetic biomembranes. Methods Enzymol **148**: 350-382

Love MI, Huber W, Anders S (2014) Moderated estimation of fold change and dispersion for RNA-seq data with DESeq2. Genome Biol **15:** 550

Lv X, Zhang Y, Zhang Y, Fan S, Kong L (2020) Source-sink modifications affect leaf senescence and grain mass in wheat as revealed by proteomic analysis. BMC Plant Biol **20**: 257

Ma Y, Ma X, Gao X, Wu W, Zhou B (2021) Light induced regulation pathway of anthocyanin biosynthesis in plants. Int J Mol Sci **22:** 11116

Mandahar C, Garg I (1975) Effect of ear removal on sugars and chlorophylls of barley leaves. Photosynthetica **9:** 407-409

Mason TG, Maskell EJ (1928) Studies on the transport of carbohydrates in the cotton plant: II. The factors determining the rate and the direction of movement of sugars. Ann Bot **42:** 571-636

Muller B, Pantin F, Génard M, Turc O, Freixes S, Piques M, Gibon Y (2011) Water deficits uncouple growth from photosynthesis, increase C content, and modify the relationships between C and growth in sink organs. J Exp Bot 62: 1715-1729

Nakata M, Mitsuda N, Herde M, Koo AJK, Moreno JE, Suzuki K, Howe GA, Ohme-Takagi M (2013) A bHLH-type transcription factor, ABA-INDUCIBLE BHLH-TYPE TRANSCRIPTION FACTOR/JA-ASSOCIATED MYC2-LIKE1, acts as a repressor to negatively regulate jasmonate signaling in *Arabidopsis*. Plant Cell 25: 1641-1656

Paul MJ, Pellny TK (2003) Carbon metabolite feedback regulation of leaf photosynthesis and development. J Exp Bot **54:** 539-547

Pertea M, Pertea GM, Antonescu CM, Chang TC, Mendell JT, Salzberg SL (2015) StringTie enables improved reconstruction of a transcriptome from RNA-seq reads. Nat Biotechnol 33: 290-295

Qin Y, Xiao Z, Zhao H, Wang J, Wang Y, Qiu F (2022) Starch phosphorylase 2 is essential for cellular carbohydrate partitioning in maize. J Integr Plant Biol **64:** 1755-1769

Quiles MJ, García C, Cuello J (1995) Differential effects of abscisic acid and methyl jasmonate on endoproteinases in senescing barley leaves. J Plant Growth Regul **16:** 197-204

Ren YH, Wang H, Harrison SP, Prentice IC, Atkin OK, Smith NG, Mengoli G, Stefanski A, Reich PB (2024). Reduced global plant respiration due to the acclimation of leaf dark respiration coupled with photosynthesis. New Phytol **241:**578-591

Rosado-Souza L, Yokoyama R, Sonnewald U, Fernie AR (2023) Understanding source-sink interactions: Progress in model plants and translational research to crops. Mol Plant **16:** 96-121

Sekhon RS, Childs KL, Santoro N, Foster CE, Buell CR, de Leon N, Kaeppler SM (2012) Transcriptional and metabolic analysis of senescence induced by preventing pollination in maize. Plant Physiol 159: 1730-1744

Sekhon RS, Saski C, Kumar R, Flinn BS, Luo F, Beissinger TM, Ackerman AJ, Breitzman MW, Bridges WC, de Leon N, Kaeppler SM (2019) Integrated genome-scale analysis identifies novel genes and networks underlying senescence in maize. Plant Cell 31: 1968-1989

Smeekens S, Ma J, Hanson J, Rolland F (2010) Sugar signals and molecular networks controlling plant growth. Curr Opin Plant Biol **13:** 273-278

Smith MR, Rao IM, Merchant A (2018) Source-sink relationships in crop plants and their influence on yield development and nutritional quality. Front Plant Sci **9:** 1889

Soualiou S, Duan F, Li X, Zhou W (2023) Nitrogen supply alleviates cold stress by increasing photosynthesis and nitrogen assimilation in maize seedlings. J Exp Bot **74:** 3142-3162

Sunil L, Shetty NP (2022) Biosynthesis and regulation of anthocyanin pathway genes. Appl Microbiol Biotechnol **106:** 1783-1798

Woo HR, Kim HJ, Lim PO, Nam HG (2019) Leaf senescence: Systems and dynamics aspects. Annu Rev Plant Biol **70:** 347-376

Wu L, Wang S, Tian L, Wu L, Li M, Zhang J, Li P, Zhang W, Chen Y (2018) Comparative proteomic analysis of the maize responses to early leaf senescence induced by preventing pollination. J Proteomics 177: 75-87

Wu T, Hu E, Xu S, Chen M, Guo P, Dai Z, Feng T, Zhou L, Tang W, Zhan L, Fu X, Liu S, Bo X, Yu G (2021) clusterProfiler 4.0: A universal enrichment tool for interpreting omics data. Innovation 2:100141

Yu S, Lo S, Ho TD (2015) Source-sink communication: regulated by hormone, nutrient, and stress cross-signaling. Trends Plant Sci **20:** 844-857

Yun D, Kang Y, Kim M, Kim D, Kim E, Hong Y (2020) Metabolomic understanding of pod removal effect in soybean plants and potential association with their health benefit. Food Res Int **138:** 109797

Zhang X, Wang M, Wu T, Wu C, Jiang B, Guo C, Han T (2016) Physiological and molecular studies of stay green caused by pod removal and seed injury in soybean. Crop J **4:** 435-443

Zhao Z, Wang C, Yu X, Tian Y, Wang W, Zhang Y, Bai W, Yang N, Zhang T, Zheng H, Wang Q, Lu J, Lei D, He X, Chen K, Gao J, Liu X, Liu S, Jiang L, Wang H, Wan J (2022) Auxin regulates source-sink carbohydrate partitioning and reproductive organ development in rice. Proc Natl Acad Sci U S A 119: e2121671119

Zhu M, Chen X, Zhu X, Xing Y, Du D, Zhang Y, Liu M, Zhang Q, Lu X, Peng S, He G, Zhang T (2020) Identification and gene mapping of the starch accumulation and premature leaf senescence mutant *ossac4* in rice. J Integr Agric 19: 2150-2164

Figure legends

Figure 1. Ear leaf phenotype and pigment content in six maize genotypes at 25 DAT under normal pollination (Ear+) and ear removal (Ear-) treatments.

(A) Leaf phenotypes of PH6WC, PH4CV, XY335, Z58, C7-2, and ZD958 at 25 DAT under Ear+ and Ear- treatments. (B-E) Contents of chlorophyll *a* (B), chlorophyll *b* (C), carotenoids (D), and anthocyanins (E) in ear leaves under Ear+ and Ear- treatments. Data are presented as means ± SEM ($n \geq 3$). ** indicates a statistically significant difference at $P \leq 0.01$ compared with Ear+ (Student's *t*-test). Scale bar = 10 cm. DAT, days after treatment.

Figure 2. Gas exchange parameters of six maize genotypes at 25 DAT.

(A) Net photosynthetic rate (P_n); (B) stomatal conductance (G_s); (C) intercellular CO_2 concentration (C_i); (D) transpiration rate (T_r); (E) dark respiration rate (R_d). Data are presented as means ± SEM ($n \geq 3$). * and ** indicate statistically significant differences at $P \leq 0.05$ and $P \leq 0.01$, respectively, compared with Ear+ (Student's *t*-test). DAT, days after treatment.

Figure 3. Chloroplast ultrastructure in bundle sheath cells (BSCs) of six maize genotypes at 25 DAT.

(A-B) Transmission electron micrographs of BSC chloroplasts under Ear+ and Ear-. (C-E) Quantification of chloroplasts (C), osmophilic granules (D), and starch granules (E) per BSC. Data are presented as means ± SEM ($n \geq 10$ independent sections obtained from four biological replicates). * and ** indicate statistically significant differences at $P \leq 0.05$ and

$P \leq 0.01$, respectively, compared with Ear+ (Student's *t*-test). Red bar = 5.0 μm. DAT, days after treatment.

Figure 4. Sucrose and starch dynamics in ear leaves of six maize genotypes following Ear+ and Ear- treatments.

(A-F) Sucrose (A-C) and starch (D-F) contents in ear leaves of PH6WC (A, D), PH4CV (B, E) and XY335 (C, F). (G-L) Sucrose (G-I) and starch (J-L) contents in ear leaves of Z58 (G, J), C7-2 (H, K) and ZD958 (I, L). Blue circles represent Ear+ treatment, and red squares represent Ear- treatment. The x-axis indicates days after treatment (DAT). Data are presented as means ± SEM ($n \geq 3$). * and ** indicate statistically significant differences at $P \leq 0.05$ and $P \leq 0.01$, respectively, compared with Ear+ (Student's *t*-test).

Figure 5. Leaf phenotypic and physiological changes in maize hybrid XY335 after Ear- and partial shading.

(A) Leaf phenotypes changes after 25 days of Ear+ (No. 1), Ear- (No. 2), and (Ear-)+ shading (No. 3-shading, No. 4 same as No. 3 after removing of the aluminum foil). (B) Chlorophyll *a*, *b*, carotenoids, and anthocyanins in the shaded part and unshaded parts. (C–F) Contents of sucrose (C), glucose (D), fructose (E), and starch (F). (G) TEM of BSCs (No.1-unshaded, No.2-shaded) and MCs (No.3-unshaded, No.4-shaded). (H–I) Number of chloroplasts (H) and starch granules (I) in BSCs and MCs. Data are presented as means ± SEM ($n \geq 5$ for (B–F), and $n \geq 20$ for (H–I)). * and ** indicate statistically significant differences at $P \leq 0.05$ and $P \leq 0.01$, respectively, compared with Ear+ (Student's *t*-test). Scale bars: red = 10 μm; blue = 2 μm.

Figure 6. Biomass accumulation and distribution in six maize genotypes at 30 DAT under Ear+ and Ear- treatments.

(A–D) Dry weight of leaves (A), stem (B), root (C), and total biomass in roots, stems, and leaves (D). Data are presented as means ± SEM (n = 10). * and ** indicate statistically significant differences at $P \leq 0.05$ and $P \leq 0.01$, respectively, compared with Ear+ (Student's t-test). DAT, days after treatment.

Figure 7. Transcriptomic analysis of four inbred lines PH6WC (W), PH4CV (V), Z58 (Z) and C7-2 (C).

(A) GO enrichment analysis. (B) Functional categorization of selected gene sets. (C) Identification and clustering of 1,673 senescence-specific DEGs (at 19 DAT), grouped by expression patterns across genotypes. (D-G) Transcriptional changes of three key candidate genes in the four inbred lines PH6WC (D), PH4CV (E), Z58 (F), and C7-2 (G), presented as $\log_2$ fold change ($\log_2$ FC) of Ear- relative to Ear+. The x-axis indicates days after treatment (DAT). (H-K) Relative expression of *ZmSWEET13a* (H), *ZmSWEET13b* (I), *ZmSWEET13c* (J), and *ZmSWEET14a* (K) at 25 DAT under Ear+ and Ear- treatments. Data are presented as means ± SEM (n = 3 for (A-G); n ≥ 3 for (H-K)). * and ** indicate statistically significant differences at $P \leq 0.05$ and $P \leq 0.01$, respectively, compared with Ear+ (Student's t-test). DAT, days after treatment. DEG, differential expression genes.

Figure 8. Proposed model of leaf phenotypic changes in response to ear removal in different maize genotypes.

After Ear- treatment, the six maize genotypes exhibited distinct leaf senescence responses: PH6WC, PH4CV, and XY335 displayed premature leaf senescence, whereas Z58, C7-2, and ZD958 maintained delayed senescence. In early-senescing genotypes, Ear- induced

significant downregulation of sugar transport (*ZmSUT*, *ZmSWEETs*) and starch metabolism (*ZmBmy3*) genes, leading to excessive starch accumulation in bundle sheath cells and sucrose buildup in mesophyll cells. This metabolic imbalance promoted anthocyanin accumulation (leaf reddening), starch granule hypertrophy, thylakoid degeneration, and eventual chloroplast lysis, collectively accelerating senescence. By contrast, delay-senescing genotypes maintained stable expression of transport and metabolic genes, supporting efficient sugar export and respiratory carbon consumption, preventing sugar overload, preserving chloroplast integrity, and sustaining normal leaf function.

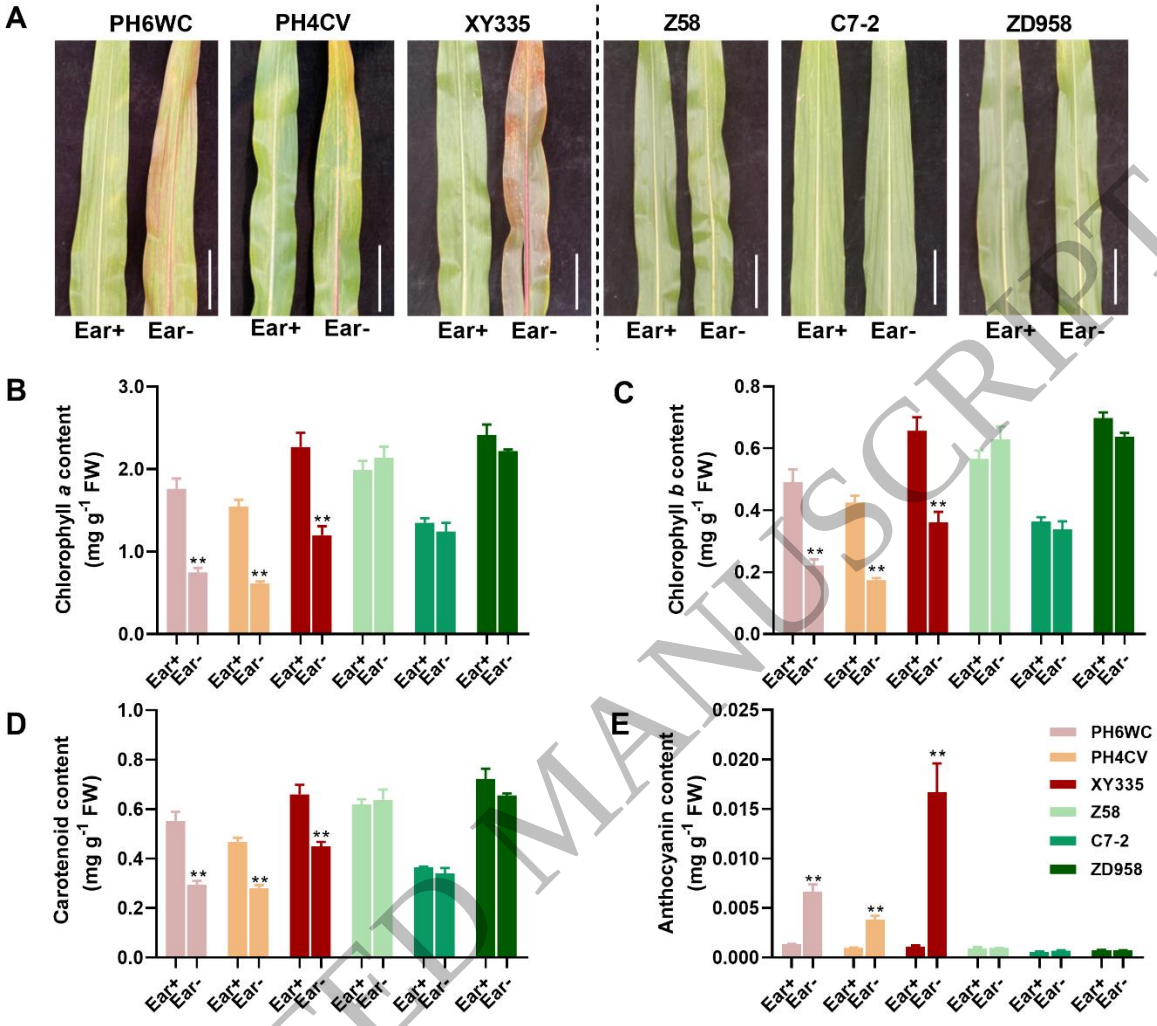

Figure 1
159x142 mm (x DPI)

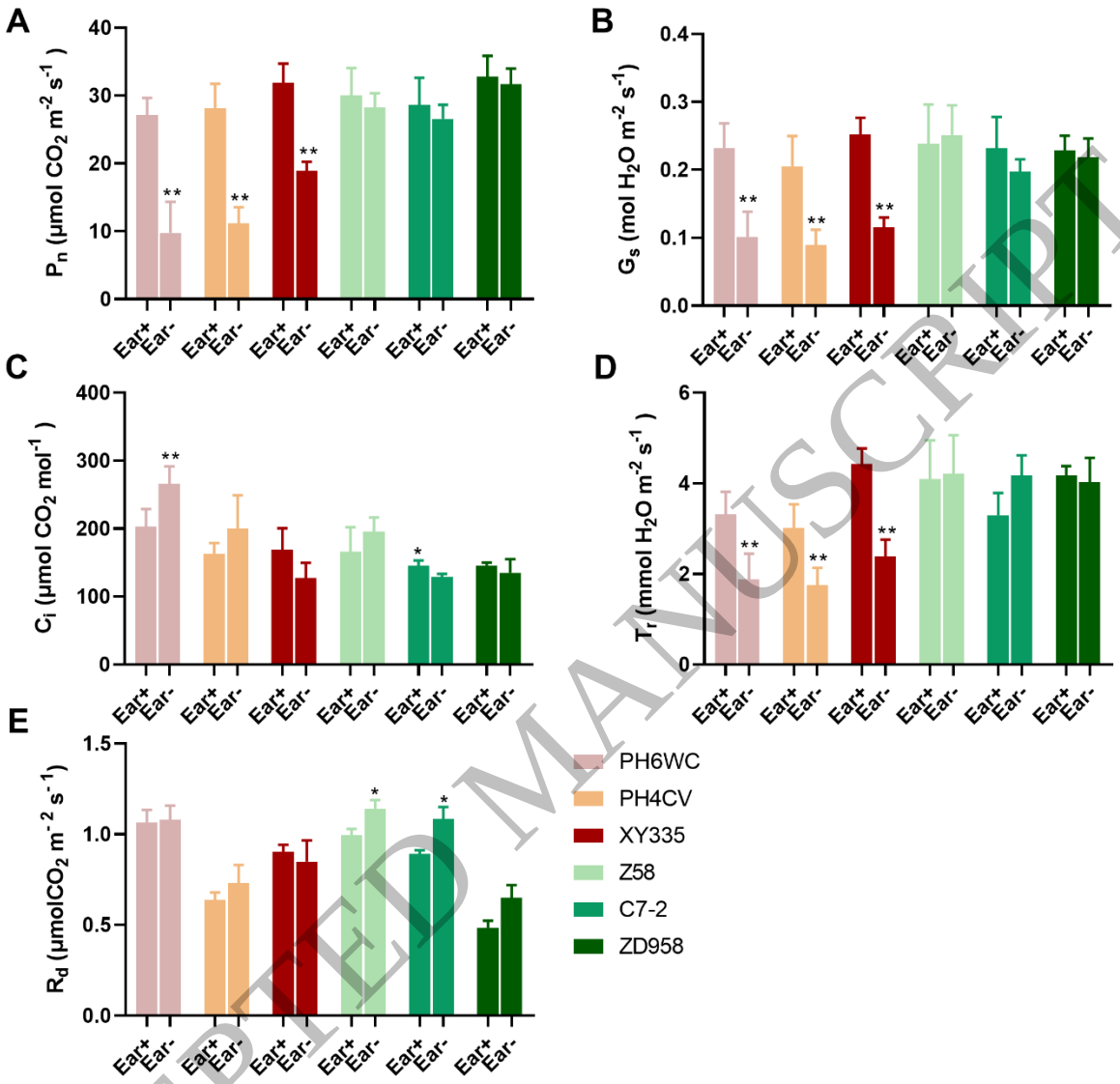

Figure 2
159x158 mm (x DPI)

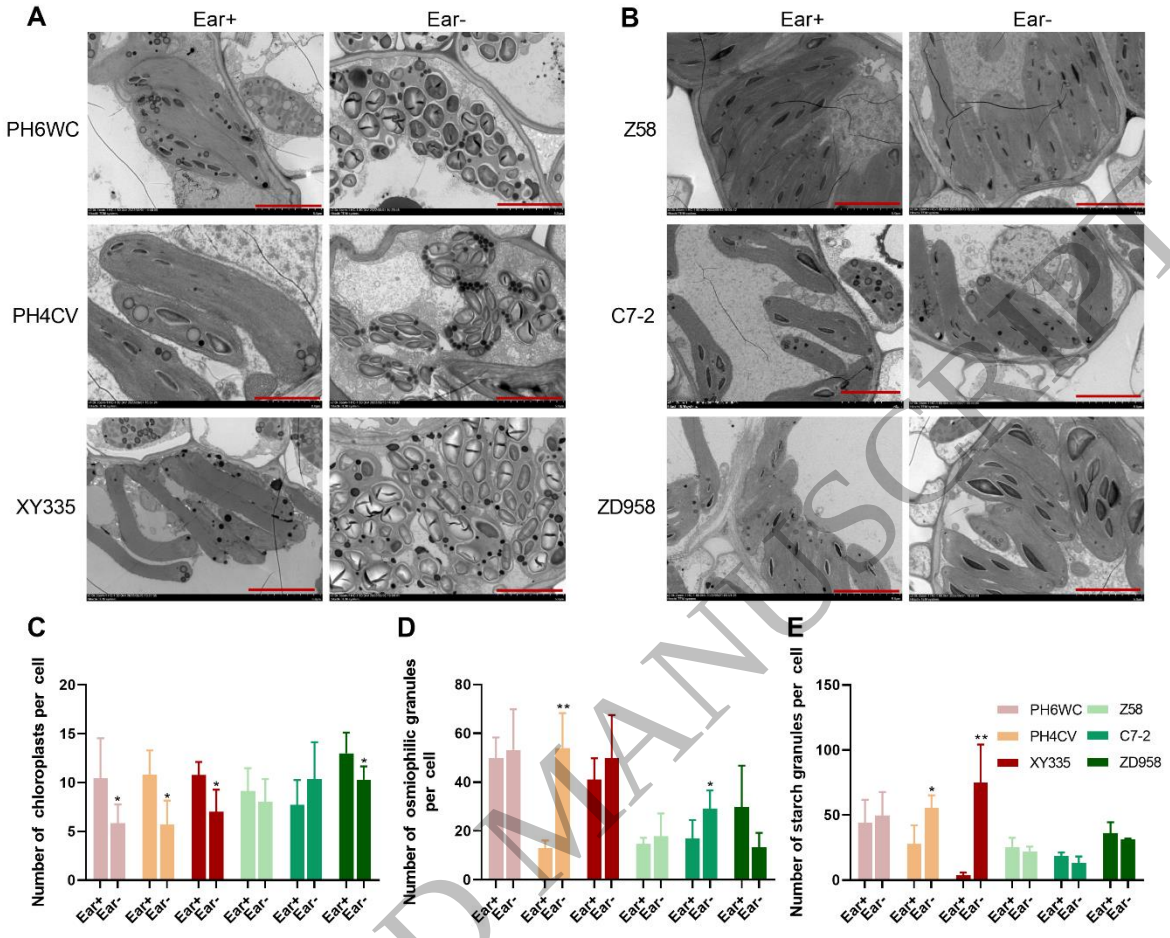

Figure 3
159x129 mm (x DPI)

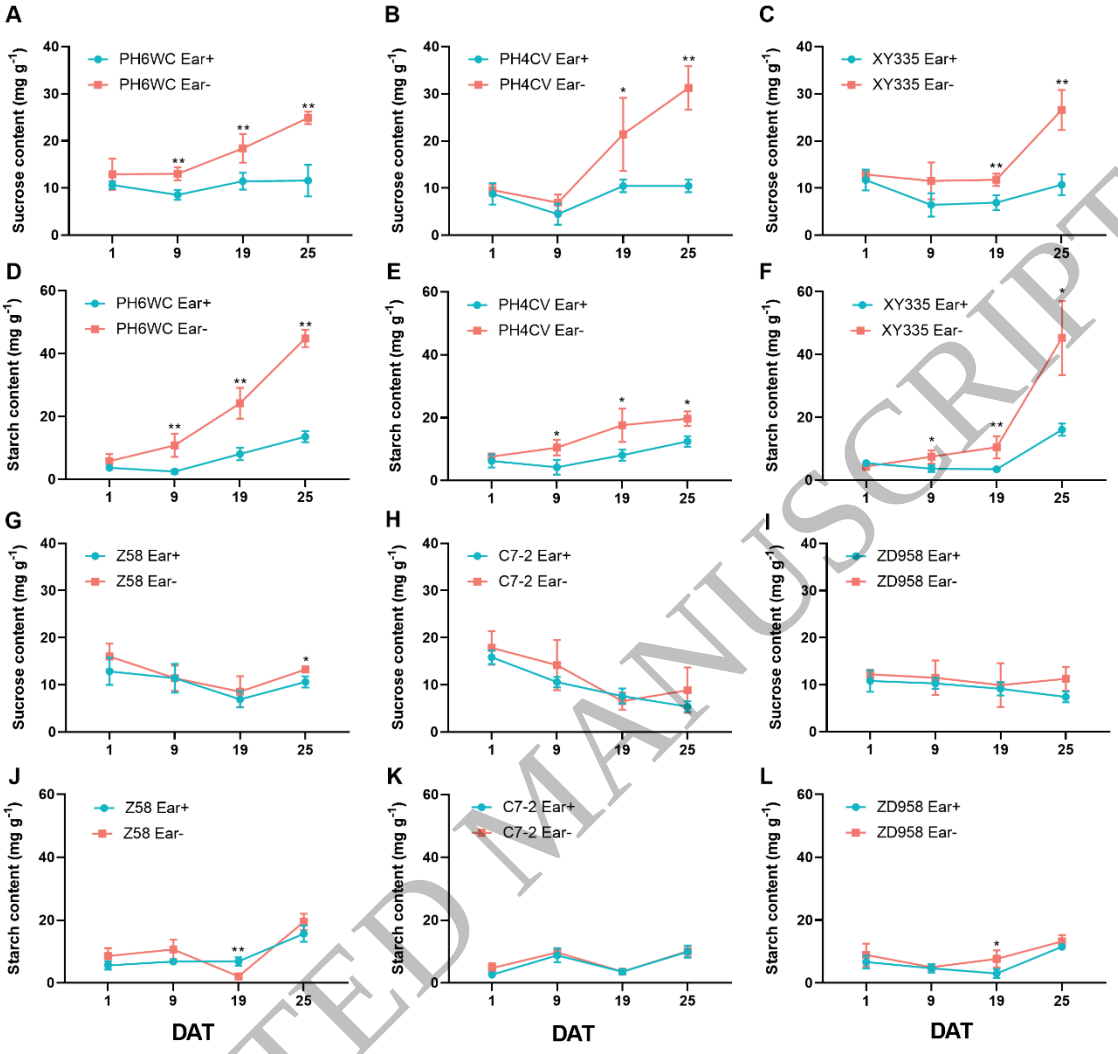

Figure 4
159x146 mm (x DPI)

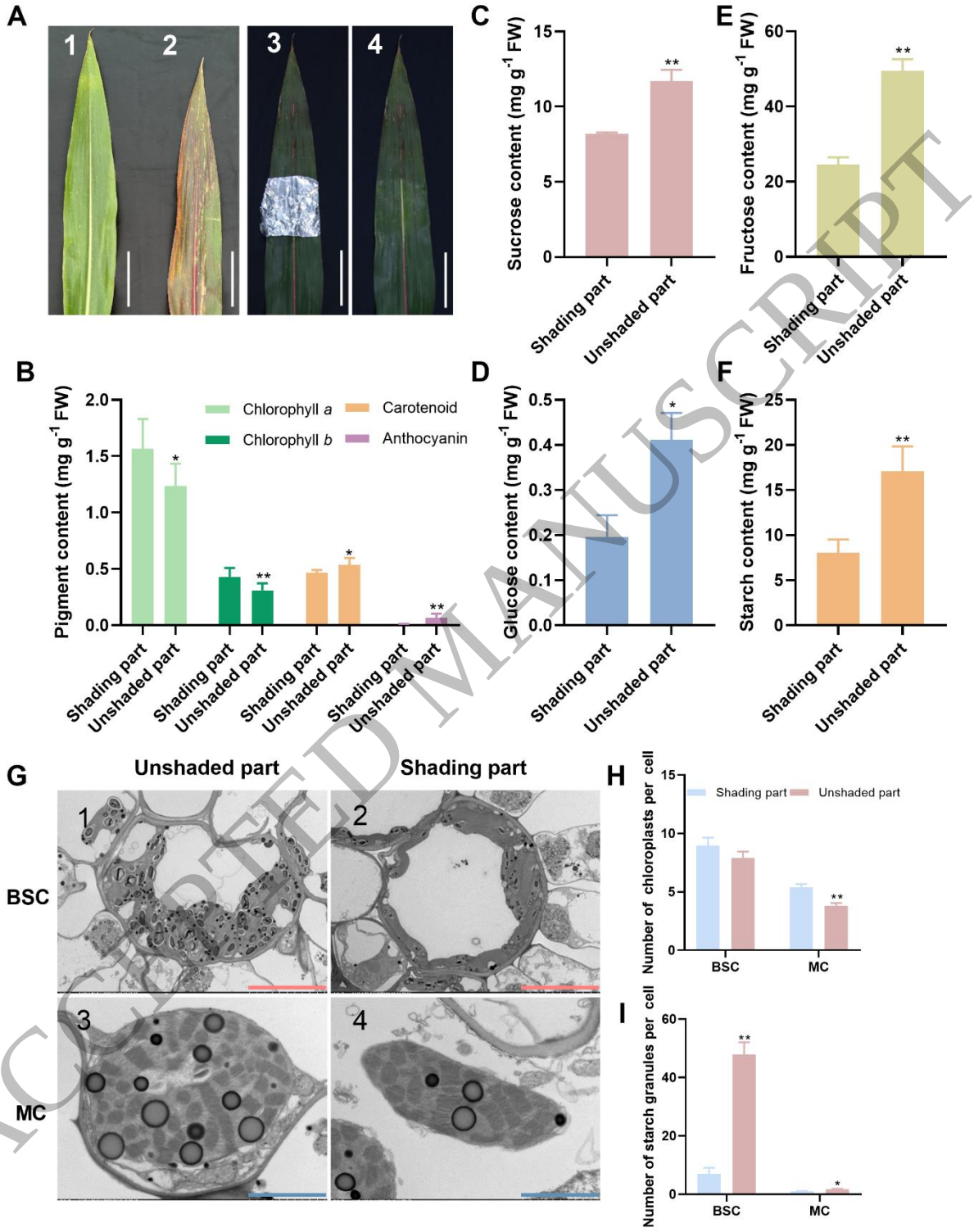

Figure 5
159x206 mm (x DPI)

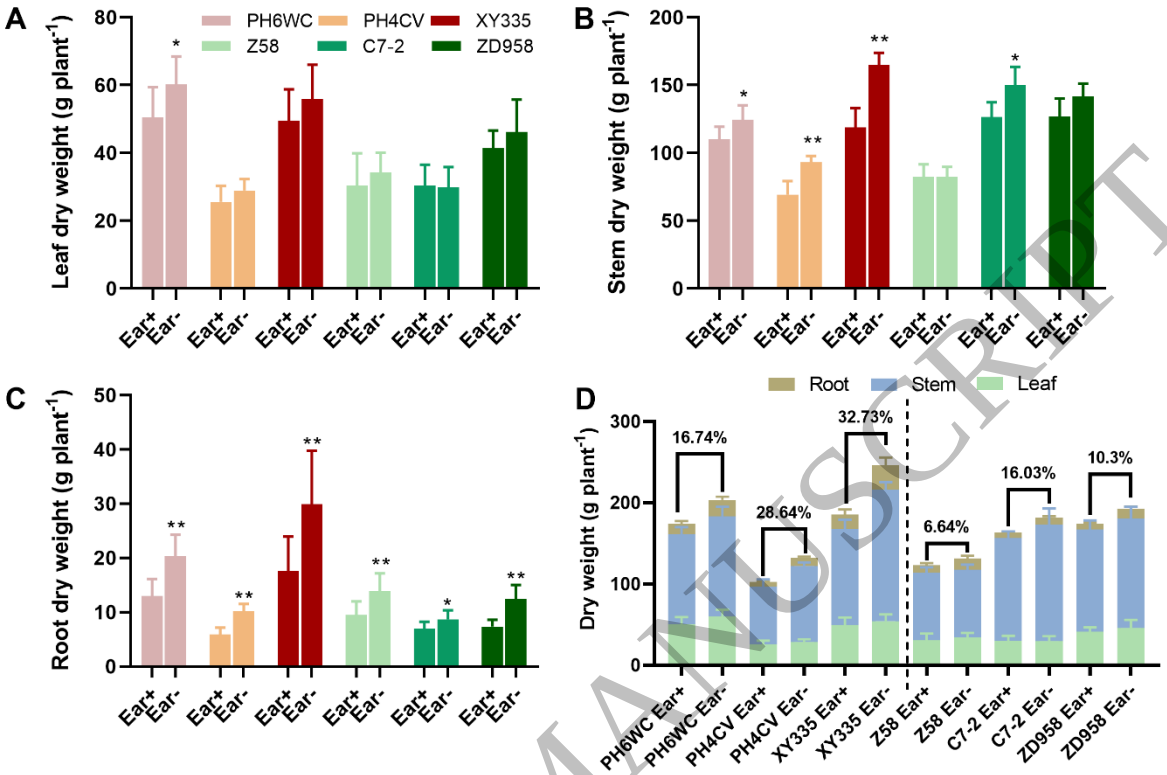

Figure 6
159x113 mm (x DPI)

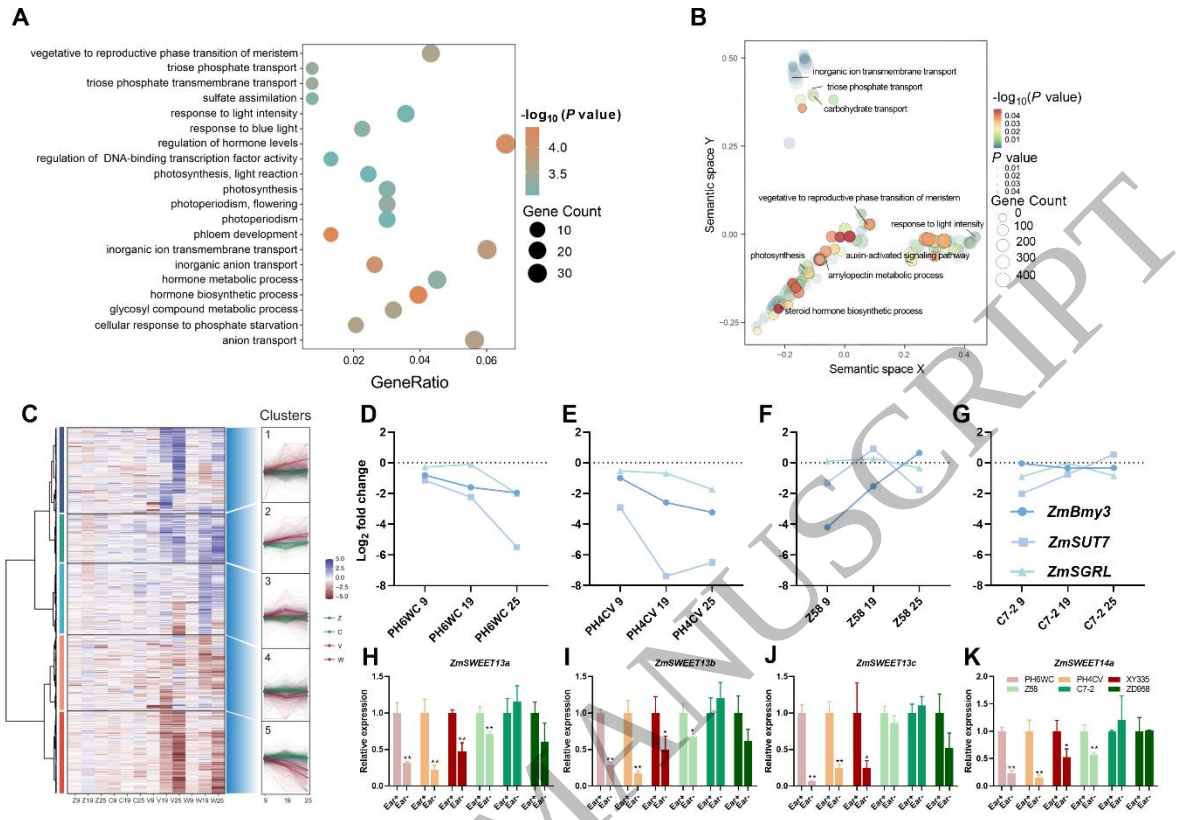

Figure 7
159x114 mm (x DPI)

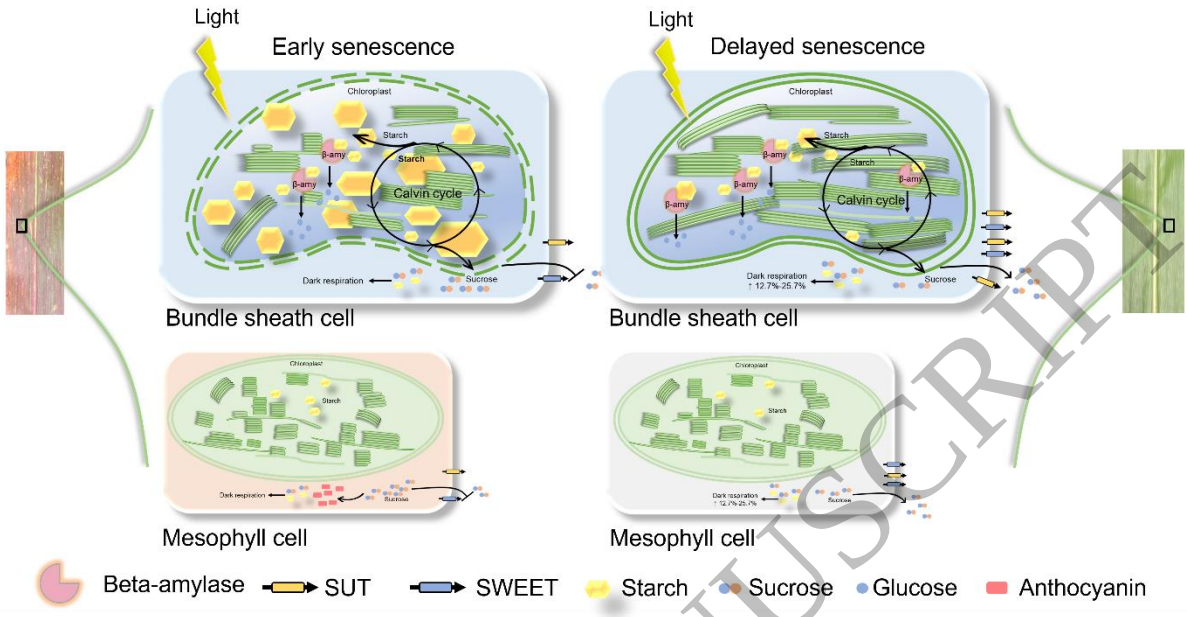

Figure 8
159x87 mm (x DPI)